Wavenumber-Domain Multiband Signal Fusion With Matrix-Pencil Approach for High-Resolution Imaging

Wang, Jianping; Aubry, Pascal; Yarovoy, Alexander

Important note
To cite this publication, please use the final published version (if applicable).
Please check the document version above.

Wavenumber-Domain Multiband Signal Fusion With Matrix-Pencil Approach for High-Resolution Imaging

Jianping Wang⬦, Pascal Aubry, and Alexander Yarovoy, *Fellow, IEEE*

Abstract—In this paper, a wavenumber-domain matrix-pencil-based multiband signal fusion approach was proposed for multiband microwave imaging. The approach proposed is based on the Born approximation of the field scattered from a target resulting in the fact that in a given scattering direction, the scattered field can be represented over the whole frequency band as a sum of the same number of contributions. Exploiting the measured multiband data and taking advantage of the parametric modeling for the signals in a radial direction, a unified signal model can be estimated for a large bandwidth in the wavenumber domain. It can be used to fuse the signals at different subbands by extrapolating the missing data in the frequency gaps between them or coherently integrating the overlaps between the adjacent subbands, thus synthesizing an equivalent wideband signal spectrum. Taking an inverse Fourier transform, the synthesized spectrum results in a focused image with improved resolution. Compared with the space–time domain fusion methods, the proposed approach is applicable for radar imaging with the signals collected by either collocated or noncollocated arrays in different frequency bands. Its effectiveness and accuracy are demonstrated through both numerical simulations and experimental imaging results.

Index Terms—Matrix-pencil approach (MPA), microwave imaging, multiband signal, signal fusion, wavenumber domain.

I. INTRODUCTION

MICROWAVE imaging has been widely used for nondestructive testing, security check, medical imaging, remote sensing, and so on. In these applications, imaging radar systems generally exploit wideband signals and antenna arrays to achieve high resolution in both downrange and cross-range directions. As downrange resolution is inversely proportional to the operational signal bandwidth of the imaging system, signals with several gigahertz or even larger bandwidth are required to achieve cm/sub-cm level resolutions, especially for short-range applications. To emit and receive such wideband signals, ultrawideband (UWB) antennas and front ends are needed. Vector network analyzers (VNAs)

and double-ridged horns often can do the job but do not satisfy end-user demands (such as size, costs, measurement speed, and so on) in numerous applications. Designing and manufacturing a UWB front ends, including antennas for a particular application, is a challenging task, especially for subsurface imaging systems such as ground-penetrating radar. To circumvent this problem, one typical solution is to split the desired operational ultrawide bandwidth into several subbands, and then relatively narrowband antennas can operate at different frequency subbands so as to cover the whole desired bandwidth. Besides the technical difficulties in UWB front ends, sometimes there might be no continuous wide/UWB spectrum available for high-resolution imaging due to the constraints of some spectrum regulations, for example, the Federal Communications Commission's radio spectrum allocation. In such circumstances, only some separate spectral bands can be used. This problem is encountered by the users of commercial UWB radar systems. Therefore, to get high-resolution UWB images, in both situations, it becomes essential to coherently process or fuse the subband signals/images acquired in different spectra.

Multiband signal fusion for improved microwave imaging has been discussed by many researchers [1]–[11]. Generally, the approaches presented in these studies can be classified into two categories: 1) signal-level fusion and 2) data-level fusion. Signal-level fusion methods directly tackle the multiband signals acquired with *monostatic/collocated radar*, which are typically implemented in the frequency domain with model-based estimation methods. For example, by exploring the f^α-type (α is the sinusoid-damping factor of the reflectivity) scattering behaviors of canonical scatterer centers over a wide bandwidth, the scattered frequency data were modeled with an autoregressive (AR) model [1] or an AR moving average (ARMA) signal model [2]. Compared with the AR model, the ARMA considers not only the poles but also the zeros of the transfer function that describes the radar returns and thus gets a more accurate estimation for the frequency-dependent scattering property (i.e., α). For the AR model, the signal poles can be estimated with a root MUltiple SIgnal Classification (MUSIC) algorithm [1], [3] and a matrix-pencil approach (MPA) [4], while for ARMA models they are obtained via singular-value decomposition (SVD) [2]. Compared with the root MUSIC and SVD-based fusion methods, the matrix-pencil-based approach achieves a better fusion performance at low signal-to-noise ratio. Moreover, recently, sparse Bayesian learning algorithms

over a constructed overcomplete dictionary [5] and the support vector regression [6] are also used to compute signal poles of the AR model. In addition, a fusion method that combines the all-phase fast Fourier transform (FT) and the iterative adaptive approach [8] was proposed to fuse the dechirped multiband signals, which is more dedicated to the linear frequency modulated signals.

On the other hand, the data-level fusion methods require a prefocusing operation for the data acquired at different positions [9], [11]. More precisely, the fusion operations are carried out on the prefocused data in the frequency–wavenumber/wavenumber domain. Therefore, it is possible to use these methods to fuse multiband signals acquired with different spatial sampling intervals in the cross-range direction, which is very attractive for many practical cases with multiband fusion imaging. For instance, in [9], AR model-based multiband coherent signal fusion processing was proposed for inverse synthetic aperture radar (ISAR) imaging. The fusion operations are performed in the frequency–wavenumber domain after the cross-range focusing operation, which alleviates the effects of the possible error caused by the bandwidth interpolation/extrapolation in the fusion processing on the cross-range response. Moreover, a matrix Fourier transform (MFT) was proposed to integrate multiple separated wavenumber domain data to implement multilook ISAR images fusion in [11]. This algorithm can also be used to integrate the multiband signals collected by different radar systems to generate a composite image. However, the frequency gaps between the different subbands are usually neglected, which could cause increased sidelobes/artifacts in the composite images.

Exploiting the advantage of the data-level fusion and also inspired by the idea for signal poles estimation in [4], we propose a wavenumber-domain (i.e., k-space [12]) multiband signal fusion algorithm with the MPA (named k-MPA) for enhanced microwave imaging. This fusion method is based on the Born approximation of the scattered field from a target resulting in the fact that in a given scattering direction, the scattered field can be represented over the whole frequency band as a sum of the same number of contributions [13]–[15]. By modeling the wavenumber-domain signals in a radial direction at different subbands as a superposition of damped/undamped exponential functions, the multiband fusion problem is converted to parameter estimation of the exponential components. Finally, taking advantage of the estimated signal models, the incoherence phase difference between the subbands can be recovered and the missing data in the frequency gap between different frequency subbands can be extrapolated to get an equivalent wide bandwidth, thus resulting in enhanced microwave images. Here, we want to specify that the proposed fusion approach uses either constant or weakly frequency-dependent scattering properties of objects over the full bandwidth for the analysis and also assumes constant velocity of wave propagation. The performance of the proposed approach for strongly frequency-dependent scatterers can be improved by using a more sophisticated model for the reflectivity functions as indicated later.
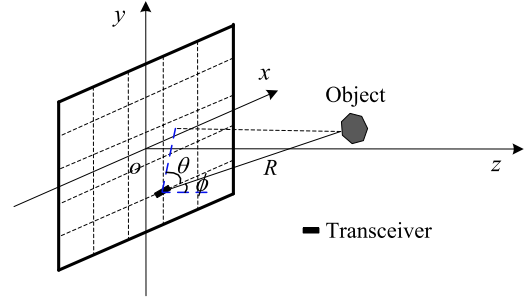

Fig. 1. Geometrical configuration of 3-D imaging. The two aspect angles θ and ϕ are defined as the angle between the line of sight and the z-axis, and the angle between the projection of the line of sight onto the xoy plane and the x-axis, respectively.

This paper is organized as follows. In Section II, the signal model in k-space is formulated and analyzed for microwave imaging. Following that, the k-space signal fusion is discussed in detail based on the MPA in Section III, which includes both signal incoherence correction and multiband signal fusion. To demonstrate the effectiveness and accuracy of the proposed approach, some numerical simulations are performed for both point targets and extended object in Section IV. Section V presents some experimental results to further validate the performance of the proposed approach. Finally, some conclusions are drawn in Section VI.

II. k-SPACE SIGNALS FOR ARRAY-BASED IMAGING

Let us consider the geometrical configuration shown in Fig. 1. A rectilinear planar antenna array is placed on the xoy plane and the object is located in the near field of the array. The transceiver position is denoted as $(x_a, y_a, 0)$. The radiated signals by each element of the antenna array can be continuous wave, pulse signal, or step-frequency signal denoted as $p(t)$ in the time domain.

Assuming the Born approximation can be applied to describe the scattered field, the signal $s(x_a, y_a, t)$ received by an antenna at (x_a, y_a) is given as

$$s(x_a, y_a, t) = \iiint_{o(x,y,z)} \frac{f(x, y, z)}{4\pi R} \cdot p(t - 2R/c) dx dy dz \tag{1}$$

where $f(x, y, z)$ is the reflectivity coefficient of a scatterer at (x, y, z), $o(x, y, z)$ is the space formed by all the scatterers, and $R = ((x - x_a)^2 + (y - y_a)^2 + z^2)^{1/2}$ is the distance between a scatterer and the antenna. Taking FT for $s(x_a, y_a, t)$ with respect to the time and two cross-range directions, the frequency–wavenumber (i.e., f-k) domain signals $S_{fk}(k_{x_a}, k_{y_a}, k)$ are obtained

$$S_{fk}(k_{x_a}, k_{y_a}, k)$$
$$= \iiint_{o(x,y,z)} f(x, y, z) P(\omega) dx dy dz$$
$$\times \iint \frac{\exp[-jkR]}{4\pi R} \exp[-j(k_{x_a} x_a + k_{y_a} y_a)] dx_a dy_a$$
$$= P(\omega) \iiint_{o(x,y,z)} f(x, y, z) \exp[-j(k_{x_a} x + k_{y_a} y + k_z z)]$$
$$\times \frac{j}{2k_z} dx dy dz \tag{2}$$

where $k = 2\omega/c$ is the wavenumber with respect to the angular frequency $\omega = 2\pi f$, k_{x_a} and k_{y_a} are the wavenumber counterparts of x_a and y_a, and $k_z = (k^2 - k_{x_a}^2 - k_{y_a}^2)^{1/2}$. $P(\omega)$ is the spectrum of $p(t)$. In the derivation of (2), the method of stationary phase is used [16].

After correcting the spectrum weighting of the radiated wavelet and compensating the wave propagation effect (i.e., propagation spreading loss) and the wavefront curvature [17], the resultant signal spectrum in the k-space can be represented as

$$S(k_{x_a}, k_{y_a}, k_z) = \iiint_{o(x,y,z)} f(x, y, z) \exp[-jk_{x_a}x - jk_{y_a}y]$$
$$\times \exp[-jk_z z]dxdydz. \quad (3)$$

In the spherical coordinate system, the wavenumbers k_{x_a}, k_{y_a}, and k_z are expressed as

$$\begin{cases} k_{x_a} = k \cos\theta \sin\phi \\ k_{y_a} = k \sin\theta \sin\phi \\ k_z = k \cos\phi \end{cases} \quad (4)$$

where θ and ϕ are the observation angles of the antenna with respect to a scatterer in the spherical coordinates and are defined as

$$\begin{cases} \phi = \arccos\left(\dfrac{z}{R}\right) \\ \theta = \arctan\left(\dfrac{y - y_a}{x - x_a}\right). \end{cases} \quad (5)$$

From (4) and (5), one can see that the point (k_{x_a}, k_{y_a}, k_z) is located on a sphere of the radius k (also known as Ewald sphere [18]), and for a specific frequency, the signal spectra of a point target lie on an arc spanned by the observation angles of the antennas with respect to the target. Meanwhile, from (4), one can see that the signal spectrum of a point target with the increase of the radar signal frequency expands along a radius of the spherical coordinate system at a specific observation angle. By setting the elevation angle ϕ to be $\pi/2$ (the target is placed in front of the antenna array), the support area of the target 2-D spectrum is a sector of a circular ring. For example, Fig. 2 shows the 2-D signal spectra of two point targets in the k-space with different frequency subbands. In addition, the combined spectrum of these two point targets is presented in Fig. 3.

Substituting (4) for k_{x_a}, k_{y_a}, and k_z, (3) can be rewritten as

$$S(k_{x_a}, k_{y_a}, k_z) = \iiint_{o(x,y,z)} f(x, y, z) \exp[-jkx \sin\phi \cos\theta]$$
$$\times \exp[-jk(y \sin\phi \sin\theta + z \cos\phi)]dxdydz$$
$$= S(k, \theta, \phi). \quad (6)$$

In a discrete form, the target signal spectrum along a particular radial direction from the origin in the k-space can be represented as

$$S(k, \theta, \phi) = \sum_{n=1}^{N} f(x_n, y_n, z_n) \exp[-jk \cdot x_n \sin\phi \cos\theta]$$
$$\times \exp[-jk(y_n \sin\phi \sin\theta + z_n \cos\phi)]$$
$$= \sum_{n=1}^{N} f(x_n, y_n, z_n) \exp[-jk \cdot d_n(\theta, \phi)] \quad (7)$$
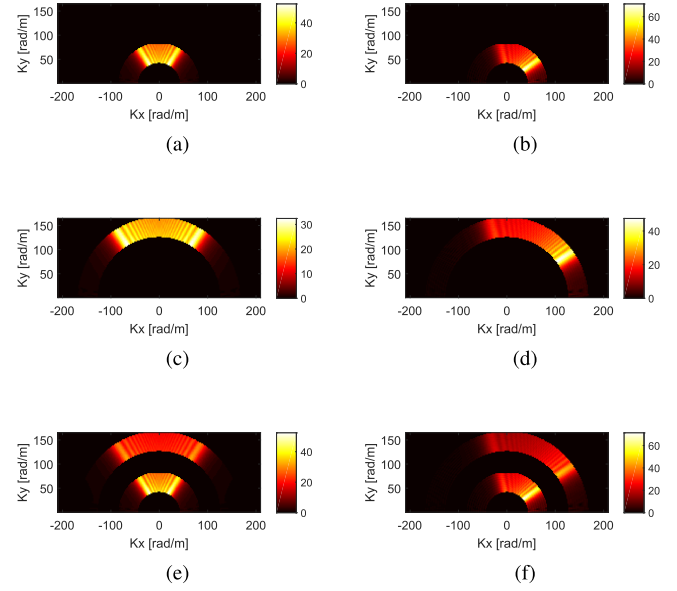

Fig. 2. Spectra of point targets in the k-space. k-space spectra of a point target opposite to the center of linear array at (a) low-frequency subband (1–2 GHz), (c) high-frequency subband (3–4 GHz), and (e) their superposition. (b), (d), and (f) Corresponding k-space spectra of a point target which is offset with respect to the center.
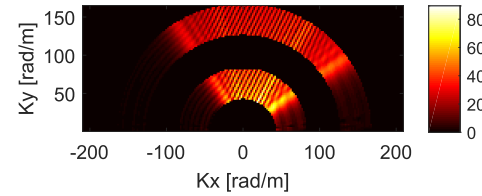

Fig. 3. k-space spectrum superposition of two point targets with both low-frequency (1–2 GHz) and high-frequency (3–4 GHz) subbands.

where

$$d_n(\theta, \phi) = x_n \sin\phi \cos\theta + y_n \sin\phi \sin\theta + z_n \cos\phi \quad (8)$$

and $f(x_n, y_n, z_n)$ is the reflectivity function of a pointlike scatterer at (x_n, y_n, z_n), N is the number of pointlike scatterers that contribute to the signal spectrum at (k, θ, ϕ) in the k-space. Note that the summation cell $\Delta V = \Delta x \cdot \Delta y \cdot \Delta z$ has been omitted in (7) for simplification. According to (5), the observation angles are just determined by the relative geometry between the antennas and the scatterers, which are independent of the signal frequency. Therefore, assuming the antenna beamwidth at all frequencies is wide enough compared to the imaging volume, at a specific aspect angle (θ, ϕ), the number of scatterers N is constant over all the frequencies. Therefore, the signals at different frequency bands share the same signal model as in (7), where the signal is expressed as a superposition of exponential components. Therefore, the multiband signal fusion can be converted to parameters estimation of exponential damped/undamped sinusoids. By estimating the number of scatterers and the reflectivity function $f(x_n, y_n, z_n)$, the signal model in (7) is obtained for a specific aspect (θ, ϕ). Then, the signal can be extrapolated based on the estimated signal model.
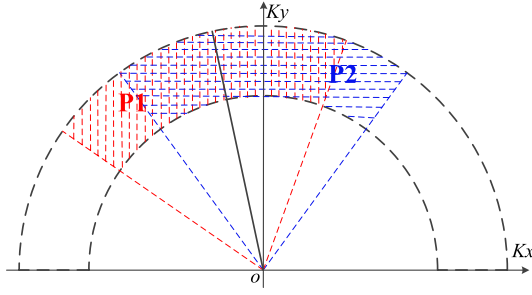
Fig. 4. Illustration of the signal spectrum in the k-space related to two point targets P1 and P2. Red-shaded area: spectrum of P1. Blue-shaded area: spectrum of P2.
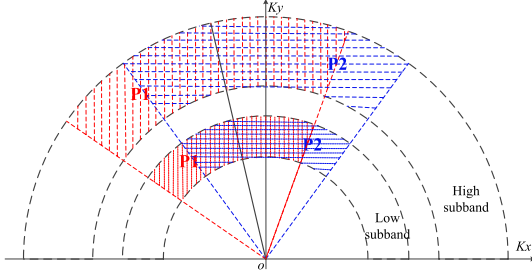

Fig. 5. Illustration of the signal spectrum in the k-space for two point targets (P1 and P2) with two subband signals. The outer angular sector is attributed to the high-frequency subband and the inner angular sector is associated with the low-frequency subband.

Such model considers the interference of the fields scattered by different voxels of the scatterer but ignores multiple scattering between different voxels. Note that the complex reflectivity function $f(x_n, y_n, z_n)$ can be modeled using different tools (for example, geometrical theory of diffraction models and exponential models) according to different scenarios. Also, frequency dependence of the material parameters of the target can be considered by the reflectivity function.

III. k-SPACE SIGNAL FUSION

For simplicity, we illustrate the principle of the k-space signal fusion in Figs. 4 and 5 for a 2-D imaging case. In Fig. 4, the effective regions of the signal spectra of two point targets, i.e., $P1$ and $P2$, are sketched. One can see that the signal spectrum of a point target in the k-space occupies an angular segment of a ring defined by the minimum and maximum radiated frequencies. The angular range of this segment is determined by the observation angles of the target with respect to the antenna array. For different point targets, different observation angles are formed and then the signal spectrum in the k-space slides along the ring according to the corresponding observation angles. Combining the signal spectra of all the individual scatterers in the k-space, we get the signal spectra for the whole imaging scene. As extended targets can be roughly considered as a composition of a group of point scatterers (voxels), a similar way is also applicable to synthesize their signal spectra in the k-space.

In terms of different radiated frequencies, the resultant signal spectrum of a point target extends along the radius within a conic sector. Fig. 5 shows the signal spectra of two point targets at two different frequency bands. Although the

signal spectra of different targets occupy different regions in the k-space (see both Figs. 4 and 5), as mentioned earlier, the signal spectra along a radial direction are attributed to the same group of scatterers for all the radiated frequencies. This lays the foundation for the k-space signal fusion to improve the image resolution.

A. Signal Incoherence Compensation

In this section, the signal model for multiband fusion is formulated. Without loss of generality, two subband signals are considered in the following. According to (7), the k-space signals in a spherical (polar) coordinate system at the low- and high-frequency subbands can be written as

$$S_1(k_1 + m\Delta k, \theta, \phi)$$
$$= \sum_{n=1}^{N} f(x_n, y_n, z_n) \times \exp[-j(k_1 + m\Delta k)d_n(\theta, \phi)] + n_1(m)$$
$$m = 0, 1, \ldots, M_1 - 1 \quad (9)$$

$$S_2(k_2 + m'\Delta k, \theta, \phi)$$
$$= \sum_{n=1}^{N} f(x_n, y_n, z_n) \exp[j(\alpha + \beta m')]$$
$$\times \exp\left[-j(k_2 + m'\Delta k)d_n(\theta, \phi)\right] + n_2(m')$$
$$m' = 0, 1, \ldots, M_2 - 1 \quad (10)$$

where $\Delta k = 4\pi \Delta f/c$ is the wavenumber counterpart of the frequency sampling interval Δf, M_1 and M_2 are the numbers of frequency samples in the two subbands, $k_1 = 4\pi f_1/c$ and $k_2 = 4\pi f_2/c$ are the wavenumbers associated with the starting frequencies f_1 and f_2 of the low- and high-frequency subbands, respectively, and $k_2 > k_1 + M_1\Delta k$. n_1 and n_2 are with zero-mean Gaussian distribution and represent measurement errors and noise. In (10), the first exponential term $\exp[j(\alpha+\beta m')]$ accounts for the phase incoherence between the two subbands. To simplify the notation, we use $S_1(m)$ and $S_2(m')$ to denote $S_1(k_1 + m\Delta k, \theta, \phi)$ and $S_2(k_2 + m'\Delta k, \theta, \phi)$ in the following. Taking some simple algebraic operations, the signals in both subbands can be rewritten as

$$S_1(m) = \sum_{n=1}^{N} f_n^{(1)} Z_n^m + n_1(m), \quad m = 0, 1, \ldots, M_1 - 1 \quad (11)$$

$$S_2(m') = \sum_{n=1}^{N} f_n^{(2)} Z_n'^{m'} + n_2(m'), \quad m' = 0, 1, \ldots, M_2 - 1$$
$$(12)$$

where

$$f_n^{(1)} = f(x_n, y_n, z_n) \exp\left[-jk_1 \cdot d_n(\theta, \phi)\right] \quad (13)$$
$$Z_n = \exp[-j\Delta k \cdot d_n(\theta, \phi)] \quad (14)$$
$$f_n^{(2)} = f(x_n, y_n, z_n) \exp[j\alpha] \cdot \exp[-jk_2 \cdot d_n(\theta, \phi)] \quad (15)$$
$$Z_n' = \exp[-j\Delta k \cdot d_n(\theta, \phi) + j\beta]. \quad (16)$$

From (13) to (16), one can see that the phase differences between the two subbands affect both the signal poles and their coefficients in (11) and (12). More specifically, the constant

phase difference influences the coefficients, while the linear phase difference term causes the rotation of signal poles over the unit circle in the complex plane. Therefore, to compensate the phase differences between the two subbands, both signal poles and their coefficients have to be estimated.

To get the signal poles and their coefficients in (11) and (12), the signal model order should be estimated first. In practice, it can be estimated by using the Akaike information criterion or Bayesian information criterion [19]. After obtaining the signal model order estimation $\hat{N}$, the signal poles can be estimated via root-MUSIC [1], estimation of signal parameters via rotational invariance techniques [20], MPA [21], and so on, while their coefficients are solved by least squares estimation. Considering the estimation accuracy and computational efficiency, we take advantage of MPA for signal pole estimation in this paper. To implement the MPA, two Hankel matrices are formed in each subband, where the measurement data, for example, S_1 are organized as

$$\mathbf{P}_1 = [\mathbf{D}_0, \mathbf{D}_1, \ldots, \mathbf{D}_{L-1}] \tag{17}$$

$$\mathbf{P}_2 = [\mathbf{D}_1, \mathbf{D}_2, \ldots, \mathbf{D}_L] \tag{18}$$

where $\mathbf{D}_i = [S_1(i), S_1(i+1), \ldots, S_1(M_1-L-1+i)]^T$, and the superscript ^{T} represents the matrix transpose. L is the matrix pencil parameter, which satisfies $\hat{N} < L < M_1 - L$. Following the suggestion in [21], we choose $L = \text{round}(M_1/3)$ here. Taking the SVD of $\mathbf{P}_1$ and $\mathbf{P}_2$ [4], we get

$$\mathbf{P}_1 = \begin{bmatrix} \mathbf{U}_1 & \mathbf{U}_1' \end{bmatrix} \begin{bmatrix} \mathbf{\Sigma}_{1,\hat{N}} & \mathbf{0} \\ \mathbf{0} & \mathbf{\Sigma}_{1,L-\hat{N}} \end{bmatrix} \begin{bmatrix} \mathbf{V}_1 & \mathbf{V}_1' \end{bmatrix}^H \tag{19}$$

$$\mathbf{P}_2 = \begin{bmatrix} \mathbf{U}_2 & \mathbf{U}_2' \end{bmatrix} \begin{bmatrix} \mathbf{\Sigma}_{2,\hat{N}} & \mathbf{0} \\ \mathbf{0} & \mathbf{\Sigma}_{2,L-\hat{N}} \end{bmatrix} \begin{bmatrix} \mathbf{V}_2 & \mathbf{V}_2' \end{bmatrix}^H \tag{20}$$

where the superscript ^{H} denotes Hermitian transpose, and $\mathbf{\Sigma}_{1,\hat{N}}$ and $\mathbf{\Sigma}_{2,\hat{N}}$ are the diagonal matrices of the $\hat{N}$ dominant singular values in the two subbands. $\mathbf{U}_1, \mathbf{U}_2, \mathbf{V}_1,$ and $\mathbf{V}_2$ are the matrices with the columns as the left and right singular vectors related to the dominant singular values. On the other hand, $\mathbf{\Sigma}_{1,L-\hat{N}}$ and $\mathbf{\Sigma}_{2,L-\hat{N}}$ are the diagonal matrices of the near-zero singular values, which represent the noise information. $\mathbf{U}_1', \mathbf{V}_1', \mathbf{U}_2',$ and $\mathbf{V}_2'$ are the matrices with the columns as the noise-associated left- and right-singular vectors. Taking the "prefiltering" operation, $\mathbf{P}_1$ and $\mathbf{P}_2$ can be approximated by their truncated SVDs denoted as $\mathbf{P}_{1T}$ and $\mathbf{P}_{2T}$, which are given as

$$\mathbf{P}_1 \approx \mathbf{P}_{1T} = \mathbf{U}_1 \mathbf{\Sigma}_{1,\hat{N}} \mathbf{V}_1^H \tag{21}$$

$$\mathbf{P}_2 \approx \mathbf{P}_{2T} = \mathbf{U}_2 \mathbf{\Sigma}_{2,\hat{N}} \mathbf{V}_2^H. \tag{22}$$

Then, we can estimate the signal poles $\{Z_n\}_{n=1}^{\hat{N}}$ of S_1 by solving the generalized eigenvalue problem $\mathbf{P}_{2T} - \lambda \mathbf{P}_{1T}$, which is also equivalent to

$$\mathbf{P}_{2T} - \lambda \mathbf{P}_{1T} \Leftrightarrow \mathbf{\Sigma}_{1,\hat{N}}^{-1} \mathbf{U}_1^H \mathbf{U}_2 \mathbf{\Sigma}_{2,\hat{N}} \mathbf{V}_2^H \mathbf{V}_1 - \lambda \mathbf{I} \tag{23}$$

where $\mathbf{I}$ is the $\hat{N} \times \hat{N}$ identity matrix. The coefficients $\{f_n^{(1)}\}_{n=1}^{\hat{N}}$ can be obtained via the least squares estimation by solving the following linear system:

$$\mathbf{S}_1 = \mathbf{A}_1 \mathbf{f}_1 \tag{24}$$

where

$$\mathbf{S}_1 = [S_1(0), S_1(1), \ldots, S_1(M_1 - 1)]^T$$

$$\mathbf{A}_1 = [\mathbf{a}_1, \mathbf{a}_2, \ldots, \mathbf{a}_{\hat{N}}]$$

$$\mathbf{a}_n = \left[1, Z_n, \ldots, Z_n^{M_L-1}\right]^T$$

$$\mathbf{f}_1 = \left[f_1^{(1)}, f_2^{(1)}, \ldots, f_{\hat{N}}^{(1)}\right]^T.$$

Therefore, the coefficients can be explicitly written as $\mathbf{f}_1 = (\mathbf{A}_1^H \mathbf{A}_1)^{-1} \mathbf{A}_1^H \mathbf{S}_1$.

Repeating the same operations with the signal S_2, its signal poles $\{Z_n'\}_{n=1}^{\hat{N}}$ and $\{f_n^{(2)}\}_{n=1}^{\hat{N}}$ can also be estimated. Then according to (14) and (16), the linear phase difference parameter β can be obtained as

$$\beta = \frac{\sum_{n=1}^{\hat{N}} \left[\text{angle}\left(Z_n'\right) - \text{angle}(Z_n)\right]}{\hat{N}}. \tag{25}$$

According to (13) and (15), the constant phase difference parameter α is obtained through

$$\alpha = \frac{1}{\hat{N}} \sum_{n=1}^{\hat{N}} \left[\text{angle}\left(f_n^{(2)}\right) - \text{angle}\left(f_n^{(1)}\right)\right]$$
$$+ \frac{k_2 - k_1}{\hat{N}} \sum_{n=1}^{\hat{N}} d_n(\theta, \phi) \tag{26}$$

where

$$\sum_{n=1}^{\hat{N}} d_n(\theta, \phi) = -\frac{1}{\Delta k} \sum_{n=1}^{\hat{N}} \text{angle}(Z_n). \tag{27}$$

Then combining (25) and (26), the incoherence phase differences of the high-frequency subband from the low subband can be compensated by

$$S_2'(k_2 + m \cdot \Delta k, \theta, \phi) = S_2(k_2 + m \cdot \Delta k, \theta, \phi)$$
$$\times \exp[-j(\alpha + m\beta)]. \tag{28}$$

Thus, the signal $S_2'(k_2 + m \cdot \Delta k, \theta, \phi)$ in the high-frequency subband is coherence-aligned with S_1 in the low-frequency subband. Note we explicitly write $S_2(m)$ as $S_2(k_2 + m \cdot \Delta k, \theta, \phi)$ to emphasize that S_2' is also a function of θ and ϕ.

B. Subband Signal Fusion

This section presents the method to fuse the multiband signals in each radial direction [i.e., (θ, ϕ)] in the k-space. Generally, the coherence-aligned subband signals can be integrated by estimating a unified signal model which then is used to extrapolate the missing data in the frequency gap between the low and high subbands. Many approaches used to fill the gap of time sequences can also be adapted to extrapolate the k-space signals. Here, we take the MPA-based iterative method [4] to fuse the k-space multiband signals. To be clear, we briefly introduce the fusion processing as follows.

After incoherence correction, the k-space coherent multiband signals, i.e., S_1 and S_2', are obtained. For the convenience

of notation, S_2' will be replaced by S_2 in the following. The common signal model of S_1 and S_2 can be expressed as

$$\tilde{S}(k_1 + m\Delta k, \theta, \phi) = \sum_{n=1}^{N} \tilde{f}_n \tilde{Z}_n^m + b(m) \qquad (29)$$

where $\{\tilde{f}_n\}_{n=1}^N$ and $\{\tilde{Z}_n\}_{n=1}^N$ are the coefficients and the signal poles, respectively, and b is the Gaussian noise. The signal poles and their coefficients in (29) can be estimated with the MPA based on S_1 and S_2. However, as a frequency gap exists between the two subbands, the two data matrices should be constructed by vertically cascading two corresponding Hankel matrices formed by the data at two subbands, which is given as

$$\mathbf{Y}_1 = \begin{bmatrix} \mathbf{P}_1^{(1)} \\ \mathbf{P}_1^{(2)} \end{bmatrix} \quad \mathbf{Y}_2 = \begin{bmatrix} \mathbf{P}_2^{(1)} \\ \mathbf{P}_2^{(2)} \end{bmatrix} \qquad (30)$$

where

$$\mathbf{P}_1^{(p)} = \left[\mathbf{D}_0^{(p)}, \mathbf{D}_1^{(p)}, \dots, \mathbf{D}_{L-1}^{(p)} \right] \qquad (31)$$

$$\mathbf{P}_2^{(p)} = \left[\mathbf{D}_1^{(p)}, \mathbf{D}_2^{(p)}, \dots, \mathbf{D}_L^{(p)} \right] \qquad (32)$$

where $\mathbf{D}_q^{(p)} = [S_p(q), S_p(q+1), \dots, S_p(M_p - L - 1 + q)]^T$, $p = 1, 2$ and $q = 0, 1, \dots, L$. Taking advantage of the MPA as presented earlier, the signal poles $\{\tilde{Z}_n\}_{n=1}^N$ and their coefficients $\{\tilde{f}_n\}_{n=1}^N$ can be obtained. Then utilizing the acquired full-band signal model in (29), the full-band signal $\tilde{S}(m)$, $m = 0, 1, \dots, M-1$, can be estimated, where M is the number of the samples in the full band with sampling intervals of Δk. To refine the estimation of the full-band signals, the similar iterative scheme as in [4] can be used. For the conciseness of this paper, the iterative scheme is omitted here.

Repeating the fusion processing in all the radial directions, coherent wideband signals are obtained in the k-space. Finally, the image reconstruction operations can be performed to get a focused image with improved resolutions.

C. More Remarks on the Implementation

The complete processing flowchart for multiband fusion imaging is shown in Fig. 6. In principle, the processing operations are divided into three major parts: 1) preprocessing for the k-space data preparation; 2) k-space signal fusion; and 3) image reconstruction, which are indicated on the left-hand side of the flowchart. The main operations for the k-space signal fusion part have been discussed in Sections III-A and III-B. The operations for the other two parts as well as some key points for the k-space fusion part are given in the following.

In the preprocessing part, as mentioned earlier, spectrum weighting effects, propagation spreading loss, and the wavefront curvature are corrected. First, spectrum weighting effects $P(\omega)$ should be compensated in the frequency domain, which is caused by the wavelet itself and the antenna transfer functions. The spectrum weighting effect introduced by the wavelet itself can be removed by multiplying the inverse of the corresponding weighting factors. The amplitude weighting effect and phase shift resulting from the antenna transfer function can be obtained by measuring the S-parameters in the calibration process and then compensated through inverse filtering.
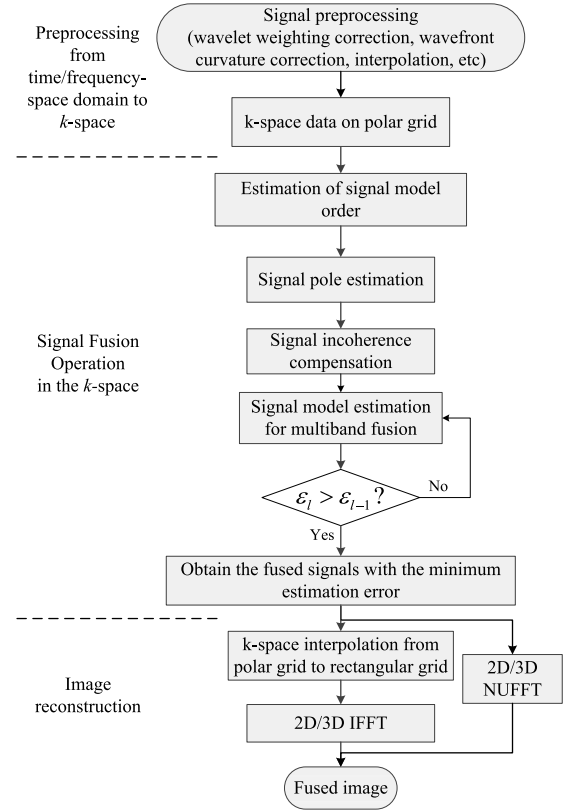

Fig. 6. Flowchart of the k-space subband fusion for imaging.

For multiband signals acquired with different antenna arrays, the possible different phase centers of antennas could affect the accuracy of the distance measurements of objects from the arrays, thus leading to misalignment of the focused images at different subbands. To avoid these possible effects, the phase centers of different antennas should be determined [22], [23] and calibrated. Next, the cross-range processing is performed to correct the wavefront curvature and propagation spreading loss. The operations are as follows. Applying the FT with respect to the cross range, the weighting-corrected signals are transformed into the frequency–wavenumber (i.e., f-k) domain. Then, the propagation spreading loss is compensated through a high-pass filter $-j2k_z$ and the wavefront curvature is corrected by Stolt-interpolation [17]. Hence, the k-space signals $S(k_{x_a}, k_{y_a}, k_z)$ for one subband are obtained. Repeating the preprocessing operations for all the subband signals, we get all their k-space counterparts. Putting all the k-space spectra in a unified coordinate system, the spectra resulting from all the subbands are obtained.

The next step is to convert the spectral data at each subband from rectilinear grid to an aligned polar grid via an interpolation, and the polar grid is given as

$$I = \left\{ (k_x, k_y, k_z) \left| \begin{array}{l} k_x = k\cos\theta\sin\phi \\ k_y = k\sin\theta\sin\phi \\ k_z = k\cos\phi \end{array} \right. \right\} \qquad (33)$$

where $k = k_1 + m\Delta k$ and $m = 0, 1, \dots, M_1 - 1$ for the low subband, while $k = k_2 + m'\Delta k$ and $m' = 0, 1, \dots, M_2 - 1$ for

the high subband. Meanwhile, $k_2 = k_1 + (M_1 + h)\Delta k$ and $h > 0$ is an integer. The observation angles θ and ϕ take uniform discrete samples, i.e., $\theta = \{\theta_0, \theta_0 + \Delta\theta, \ldots, \theta_1\}$ and $\phi = \{\phi_0, \phi_0 + \Delta\phi, \ldots, \phi_1\}$, where θ_0 and θ_1 and ϕ_0 and ϕ_1 are the minimum and maximum values of the observation angles θ and ϕ, respectively; $\Delta\theta$ and $\Delta\phi$ are their corresponding sampling intervals. To avoid aliasing of the focused image in the space domain, the sampling intervals Δk, $\Delta\theta$, and $\Delta\phi$ should satisfy

$$\begin{cases} \Delta k \le 2\pi/d_{\max} \\ \Delta\theta \le \lambda_{\min}/(4 \cdot r) \\ \Delta\phi \le \lambda_{\min}/(4 \cdot r) \end{cases} \quad (34)$$

where $d_{\max}$ is the largest dimension of the imaging scene in the range direction. $\lambda_{\min}$ is the wavelength corresponding to the highest frequency, and r is the maximum cross-range radius of the imaging scene (i.e., the minimum radius of a cylinder with its axis along the downrange that encloses the imaging scene).

In addition, we have to mention that the cross-range focusing can also be implemented in the time–space domain via Kirchhoff migration [24], which actually leads to focused images. Then applying IFT to the focused images, the k-space spectra associated with each subband are obtained. The rest of the operations keep the same.

After getting the k-space spectra on an aligned polar grid (as shown in Fig. 3 or 5), the k-space signal fusion is carried out along each radial direction with the matrix pencil-based approach presented in Sections III-A and III-B. After obtaining the fused signals in the k-space, a 2-D/3-D interpolation is needed to convert the data from the polar grid to a rectilinear grid. Then, an inverse FT is applied to the k-space data to reconstruct an image in space. Furthermore, to improve the computational efficiency, the interpolation operation and the inverse FT can be replaced by a 2-D/3-D nonuniform fast FT operation [25], [26], which was actually used for the image formation in this paper.

IV. NUMERICAL SIMULATION

Without loss of generality, in the following, we use two-band signal fusion to demonstrate the proposed approach to short-range imaging via both numerical simulations and experimental measurements.

A. Point Targets

First, a numerical simulation was performed for point targets with two-band signals. The simulation parameters are listed in Table I. Assume the antenna array was placed on the x-axis with its center at the origin and the y-axis pointing toward the illuminated scene. The antenna array was 2 m in length and operated in two separate bandwidths, namely, 2–4 and 6–8 GHz. Four point targets (i.e., small spheres of radius 1 cm) were placed in front of the antenna array at the positions $(-0.5, 1)$, $(0, 0.95)$, $(0, 1.05)$, and $(0.4, 1.2)$ m, respectively. The Hertz dipole was used as the radiator in the antenna array, and the interelement spacings of antennas

TABLE I
SIMULATION PARAMETERS FOR POINT TARGETS

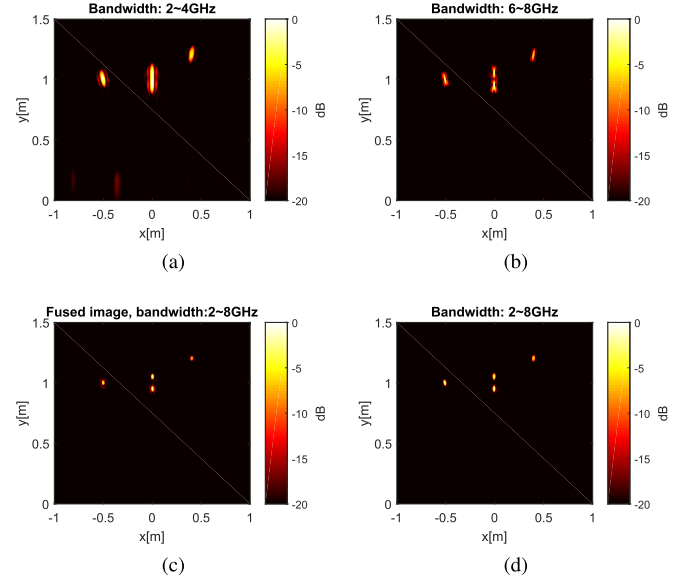|	Parameter	Value
	Low-frequency band	2–4 GHz
	High frequency band	6–8 GHz
	Antenna aperture	2 m
Case 1	Element spacing of low-freq antenna	1 cm
	Element spacing of high-freq antenna	1 cm
Case 2	Element spacing of low-freq antenna	2 cm
	Element spacing of high-freq antenna	1 cm

Fig. 7. Image fusion of point targets. (a) and (b) Images of point targets with the bandwidths of 2–4 and 6–8 GHz, respectively. (c) Fused image with the bandwidth of 2–8 GHz. (d) Reference image obtained with the bandwidth of 2–8 GHz.

were 1 cm at both bandwidths (see Case 1 in Table I). The electromagnetic (EM) data at the two bandwidths were synthesized by the commercial EM software FEKO with the full-wave solver method of moments in the frequency domain with the frequency steps of 20 MHz.

Taking advantage of the range migration algorithm [17] for image formation with the EM data at the two frequency subbands, the focused images were obtained, as shown in Fig. 7(a)–(c). The two focused images with the bandwidth of 2–4 and 6–8 GHz are presented in Fig. 7(a) and (b). As the same antenna aperture was used for both low- and high-frequency band signals, high-frequency band signal results in finer cross-range resolution of the focused image compared with the low-frequency band signal. In the downrange direction, the similar resolutions are achieved for both high-and low-frequency signals as their bandwidths were equal. Fig. 7(c) shows the focused image by fusing the EM signals of the bandwidth 2–4 and 6–8 GHz with the proposed fusion method. As an equivalent bandwidth of 2–8 GHz is achieved in the fused image, we can see that in Fig. 7(c), the two point targets on the y-axis are more clearly resolved than those in the two subband images [see Fig. 7(a) and (b)]. For comparison,
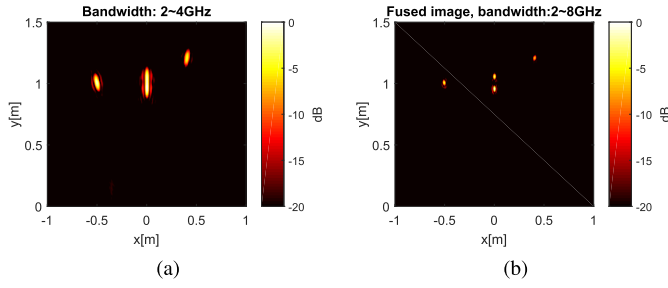
Fig. 8. Signal fusion of point target with noncollocated antennas in low- and high-frequency subbands. (a) Low-frequency images acquired with a downsampled linear array. (b) Fusion image with the signals collected by downsampled low-frequency array and the same high-frequency array as in Fig. 7.
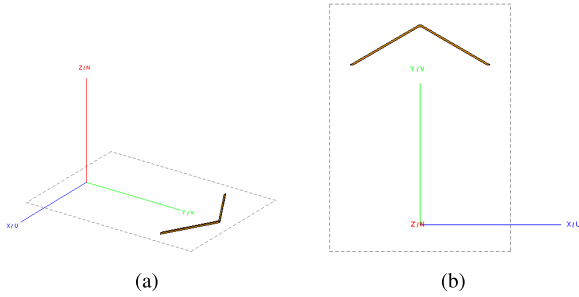

Fig. 9. Geometrical configuration for extended target simulation. (a) 3-D geometry. (b) Top view against the z-axis.

the focused image with the EM data of the full bandwidth 2–8 GHz is shown in Fig. 7(d). One can see that the fused image is comparable to the real image reconstructed with wideband signals in terms of the spatial resolution.

In practical imaging systems, the element spacing of low-frequency array is generally larger than that of high-frequency array. To emulate this, we kept the element spacing of high-frequency array but doubled the sampling intervals (i.e., downsampled the spatial samples by a factor of two) of the low-frequency array for a second experiment (Case 2 in Table I). After the image formation, the EM signals collected with the downsampled low-frequency array were focused and the image is shown in Fig. 8(a), which is comparable to Fig. 7(a). As in Case 2, the EM signals synthesized with the high-frequency antenna array were the same as that in Case 1, and the same image was obtained as Fig. 7(b) that we omit here for the conciseness of this paper. Applying the proposed fusion approach to the signals in low- and high-frequency subbands, a fused wideband image was obtained again, as shown in Fig. 8(b). One can see that the image in Fig. 8(b) is nearly the same as that in Fig. 7(b) and the two point targets on the y-axis are well resolved again compared to those in the two subband images.

B. Extended Object

An extended target was also used for a numerical experiment to further validate the proposed approach. The extended target was a "V"-shaped perfect electric conductor object (see Fig. 9). The two bars of the object are 20.16 cm in
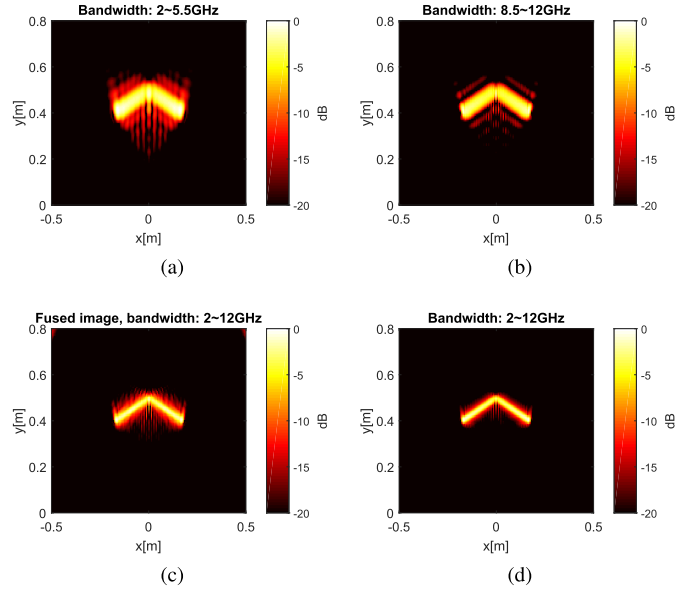

Fig. 10. Image fusion for extended target. (a) and (b) Focused images of the cornerlike scatterer with the bandwidth of 2–5.5 and 8.5–12 GHz, respectively. (c) Fused image of the cornerlike scatterer with the bandwidth of 2–12 GHz. (d) Reference image obtained with the bandwidth of 2–12 GHz.
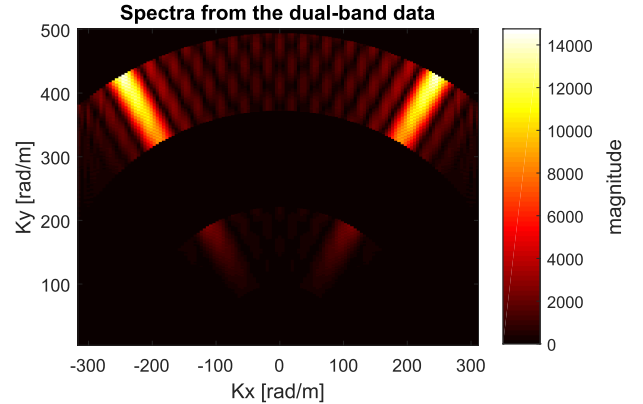

Fig. 11. k-space spectra from the dual-band data. The spectrum at the bottom of the figure results from the low-subband data, while the top from high subband.

length and 5 mm in both width and thickness, and they form an obtuse angle of 120.5°. A linear antenna array formed by Hertz dipoles was used as the radiator for 2-D image formation. The linear antenna array was set along the x-axis with its center at the origin and the "V"-shaped object was placed on the xoy plane at a distance of 0.4 m from the array, as shown in Fig. 9. The linear array was 1 m in length with the element spacings of 1 cm. The operational bandwidths, i.e., 2–5.5 and 8.5–12 GHz, were utilized as the low- and high-frequency signal bands. The EM synthetic data for the two operational bandwidths were also generated by the EM software FEKO in the frequency domain with the frequency steps of 100 MHz.

The EM synthetic data in the two operational bands were focused with range migration algorithm [17] and the reconstructed images are shown in Fig. 10(a) and (b). As for point
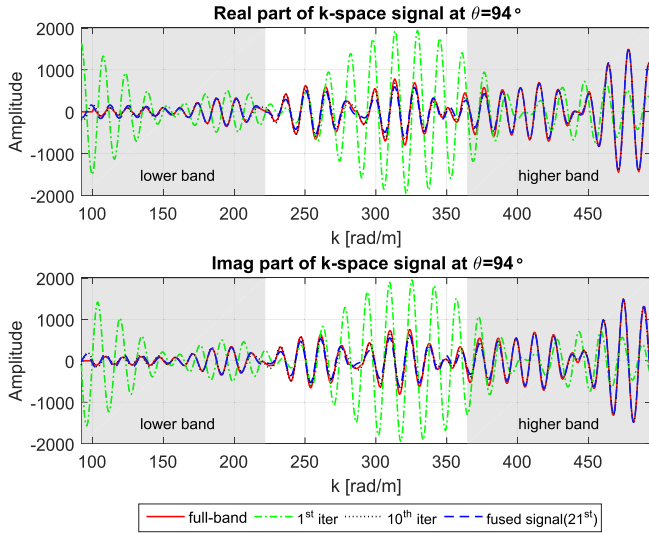
Fig. 12. Real and imaginary parts of the original k-space signal and the fused signal at the aspect angle $\theta = 94°$. Here the "ith iter" refers to the estimated signal after the ith iteration. Shaded parts: data at the low- and high-frequency subbands.

targets, the downrange resolutions of the two reconstructed subband images are relatively coarse and strong artifacts around the target are also observed in the images. Exploiting the two-band signals and taking advantage of the proposed fusion approach, a higher downrange resolution is achieved in the fused image [see Fig. 10(c)] where the strong artifacts appeared in the subband images are significantly suppressed. To examine the quality of the fused UWB image, the focused image with the entire bandwidth of 2–12 GHz is shown as a reference in Fig. 10(d). Comparing Fig. 10(c) and (d), the fused image achieves the similar downrange resolution as that of the reference one. However, slight differences are noticed in the sidelobe levels in the two images. This may be caused by the estimation errors of the fused signals with respect to the real full-band signals in the k-space. Nevertheless, these differences in the sidelobe levels have little influence on the target detection and recognition. Therefore, a satisfactory image was obtained by fusing the data of the two frequency subbands.

To explicitly show the accuracy of the fusion method, we compared the fused signals and the original ones. The k-space spectra of the "V"-shaped object from the dual-band data are displayed in Fig. 11. Fig. 12 shows the fused signal and the original one at an aspect angle of $\theta = 94°$, where the original full-band signal is obtained after some preprocessing for the full-band synthetic EM data. Although slight differences may be noticed at some points, it can be seen that the fused signal agrees with the original one very well. Moreover, some estimated signals during the iterations are also shown in Fig. 12 to demonstrate the convergence of the iterative scheme. At the beginning of the iterations, one can see that the estimated signal (i.e., the first iter) oscillates with the similar frequencies as the original full-band signal, but its amplitude is significantly different from that of the original one. After 10 iterations, the amplitude of the oscillated signal converges to the original one (see both the real and imaginary
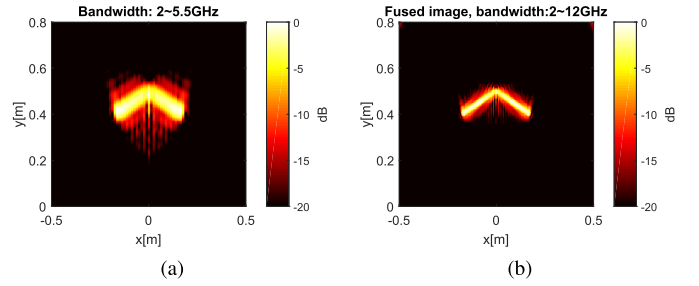

Fig. 13. Fusing signals acquired by noncollocated low- and high-frequency antennas for extended target. (a) Focused low-frequency image with the antenna element spacing of 2 cm at 2–5.5 GHz. (b) Fused image with the bandwidth of 2–12 GHz.

parts of the signals). By minimizing the difference between the estimated and the measured signals, the finally fused signal at this aspect angle was obtained after 21 iterations. One can see that the signal converges very fast to a relatively accurate estimation after the first several iterations, but it takes more iterations to reach the minimum difference between the estimated signals and the measured ones at the two frequency subbands.

Similar to the point targets' simulation, we took every other spatial sample of the linear array (i.e., element spacing of 2 cm) for the low-frequency subband to emulate the different element spacings of the low- and high-frequency antenna arrays in practical imaging systems. The focused image for the signals acquired with the downsampled low-frequency linear array is shown in Fig. 13(a), which is nearly identical to the low-subband image in Fig. 10(a). Again, the same image as that in Fig. 10(b) was obtained with high-frequency subband signals and we omit it here. Taking the fusion operation for the two subband signals in the k-space, a focused image with the enhanced resolution was acquired. Fig. 13(b) presents the fused image with the bandwidth of 2–12 GHz. It is visually equivalent to that in Fig. 10(c) fused with the signals acquired by collocated low- and high-frequency antenna arrays. Moreover, this fused image [see Fig. 13(b)] is comparable to the full-band image in Fig. 10(d), especially in terms of the spatial resolutions. Therefore, one can see that the proposed k-space fusion method works effectively for the signals acquired with noncollocated antenna arrays as well.

In addition, it should be mentioned that the Born approximation used for the formulation is not precisely met in this circumstance (where the Kirchhoff approximation is theoretically more appropriate for metallic objects or strong scatterers [27]); however, a relatively well-reconstructed profile of the "V"-shaped target is still obtained with the proposed approach. Therefore, this numerical simulation also shows the robustness of the proposed approach for the shape reconstruction of a broad range of scatterers.

V. EXPERIMENTAL RESULTS

Experimental measurements were carried out in the anechoic chamber for further demonstration. The experimental setup is shown in Fig. 14(a). A Vivaldi antenna [28] with the operational frequency band from 2.7 to 35 GHz was used as a transceiver, as shown in Fig. 14(c). It was fixed on a planar scanner with polyethylene foam and connected to a VNA.
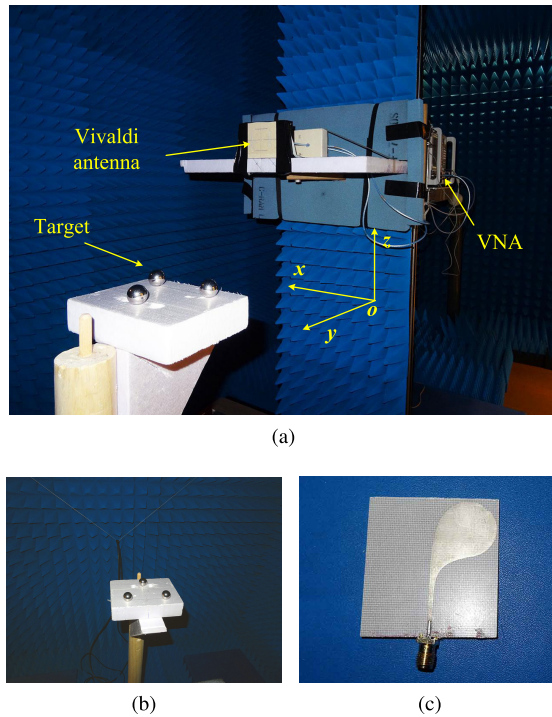
Fig. 14.   (a) Experimental setup. (b) Metallic sphere targets. (c) Antipodal Vivaldi antenna used for the measurement.

With the translation of the planar scanner, the transceiver antenna took samples over the xoz plane to synthesize a rectilinear aperture of the dimensions of 0.5 m × 0.5 m. The spatial sampling intervals of the antennas in both the x- and z-directions are 1 cm. Three metal spheres of diameter 2 cm were placed on the xoy plane in front of the array center. The two nearer spheres were separated with an interval of 10 cm and placed at a distance of 54.3 cm away from the antenna aperture. The third sphere was set 7 cm further away than the center of gravity of the other two. Two subband signals with the operational frequencies ranging from 4 to 7 and 11 to 14 GHz, respectively, were used. The signals were measured in the frequency domain with the steps of 20 MHz by the VNA. In addition, calibration was done before taking the measurement to eliminate the reflections between the VNA and the antenna.

Then, the acquired EM data were focused with range migration algorithm for the two subband signals. The formed 3-D images as well as their projection views are shown in Fig. 15(a)–(h). In both low- and high-frequency subbands, the images of spheres are relatively well reconstructed. Thanks to the short wavelengths of the high-frequency signals, a finer cross-range resolution is achieved in the high-frequency image [see Fig. 15(f) and (h)]. On the other hand, the equal coarse downrange resolutions are obtained in the images of both subbands due to the equal signal bandwidths (i.e., 3 GHz).

To improve the downrange resolution, the signals acquired in both low- and high-frequency subbands are processed and fused in the k-space by using the proposed approach. The fused images are shown in Fig. 15(i)–(l). One can see that

the images of objects are well focused in the fused image and the downrange resolution along the y-axis is noticeably improved compared to that of the images reconstructed with each individual subband (i.e., 4–7 and 11–14 GHz). For comparison, the two subband signals are also fused with the MFT approach proposed in [11] and the fused images are shown in Fig. 15(m)–(p). One can see that the fused image is focused very well in the cross-range direction [see Fig. 15(n)] and the downrange resolution is improved [see Fig. 15(o)–(p)]. However, split main lobes are observed along the downrange direction. This results from the fact that in the MFT approach, the k-space data from different subbands are only registered in an aligned coordinate system without any operation to deal with the missing data in the frequency gap. Hence, split main lobes are obtained. In contrast, the MPA-based method not only coherently registers the k-space data but also extrapolates the missing data to fill the frequency gap, which leads to the sharply focused main lobe and enhances the downrange resolution.

As a benchmark, the images focused with the fully measured data within the bandwidth 4–14 GHz (i.e., full-band images) are also shown in Fig. 15(q)–(t). Compared with the benchmark images in Fig. 15(q)–(t), the fused images achieve comparable image qualities, especially in terms of the downrange resolution [see Fig. 15(i)–(l)]. However, relatively high sidelobes are observed in the fused image and the sphere at the further position exhibits weaker intensity in the fused image than that in the full-band images. This is mainly caused by the differences between the estimated data and the real data in the frequency gap. As in the fusion process, the reflectivity functions were assumed to be constant over the entire signal bandwidth, i.e., frequency-independent. Based on this assumption, a signal model was estimated with the measured data in the low- and high-frequency subbands. Using the estimated signal model, the missing data in the frequency gap between the low- and high-frequency bands were extrapolated. Consequently, an equivalent full-band data were obtained by combining low-frequency, high-frequency, and extrapolated data for high-resolution imaging. Nevertheless, the reflectivity functions of practical targets can never be absolutely frequency-independent. Therefore, extrapolated data in the frequency gap may have some differences from the real one, thus resulting in the slight difference in the focused image. To be more accurate in capturing the features of the reflectivity functions of targets, a more advanced model should be used to characterize the targets' scattering signatures over a wide bandwidth, e.g., the state-space-based modeling [2], [29].

Although the background reflections and clutters were almost perfectly eliminated by taking the experimental measurement in the anechoic chamber, which suppresses their impact on the fusion of the scattered signals from the targets, the suggested fusion method should work as well with their presence. This is because the background reflections also follow the same fact that the k-space signals along a radial direction from the origin are attributed to a set of scatterer (including the background scatterers) in the imaging scene. With the presence of background reflections, the only
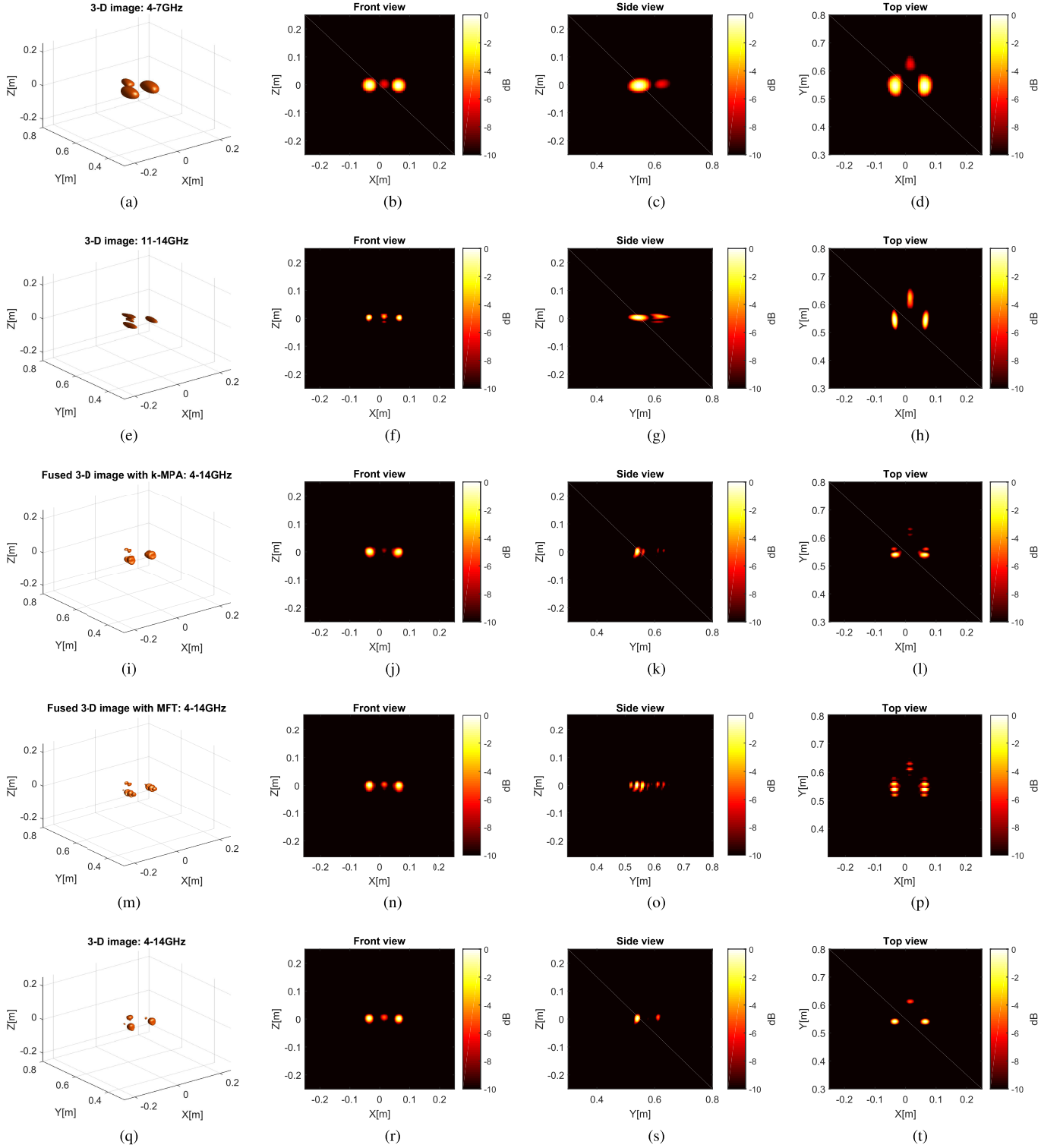
Fig. 15. Focused images with two subband signals and the whole bandwidth. (a)–(d) 3-D image and its projection views on the *xoz*, *yoz*, and *xoy* planes for the low-frequency signal (4–7 GHz). (e)–(h) 3-D image and its projection views on the three planes for high-frequency signal (11–14 GHz). (i)–(l) Fused 3-D image with the proposed method and its projection views on the three planes for the full-band signal (4–14 GHz). (m)–(p) Fused 3-D image with the MFT method and its projection views on the three planes for the full-band signal (4–14 GHz). (q)–(t) 3-D image and its projection views on the three planes for the real full-band signal (4–14 GHz). All 3-D images show the isosurfaces of −10 dB in the focused volume.

consequence is that the signals from background scatterers are also fused. Thus, the corresponding background scatterers also appear in the fused images at appropriate places (outside the target area) and with improved resolution.

VI. Conclusion

In this paper, we propose a matrix-pencil-based approach to fuse multiband signals in the wavenumber domain (i.e., *k*-space) for high-resolution microwave imaging. The proposed

approach fuses the multiband data along each radial direction in a spherical (or polar) coordinate system in the k-space for 3-D (or 2-D) imaging after some preprocessing (i.e., wavelet spectrum weighting compensation and wavefront curvature correction). Through the fusion operation, the k-space spectrum corresponding to an equivalent (ultra-)wideband signal is formed, which leads to resolution-enhanced images after focusing. Thanks to its operations in the k-space, the proposed fusion method works for the data collected by either collocated or noncollocated antennas in different frequency bands. As the proposed approach is based on the Born approximation, its applicability is limited by the Born approximation applicability, which is widely discussed in the open literature. Although the method was formulated based on the wave propagation in a lossless homogeneous medium, the proposed approach could also be readily extended to, for instance, through-wall imaging applications by exploiting proper Green's functions [30]. However, when the medium has strong attenuation or/and dispersion effects, the proposed approach would fail as distortions of the amplitudes or/and phases of signals introduced during the wave propagation were neglected. To address the multiband signal fusion problem in such circumstances, both attenuation and dispersion effects of the medium should be considered to develop a modified version of the proposed approach in the future.

REFERENCES

[1] K. M. Cuomo, J. E. Pion, and J. T. Mayhan, "Ultrawide-band coherent processing," *IEEE Trans. Antennas Propag.*, vol. 47, no. 6, pp. 1094–1107, Jun. 1999.

[2] J. E. Piou, K. M. Cuomo, and J. T. Mayhan, "A state-space technique for ultrawide-bandwidth coherent processing," DTIC, Fort Belvoir, VA, USA, Tech. Rep. 1054, 1999.

[3] B. Tian, Z. Chen, and S. Xu, "Sparse subband fusion imaging based on parameter estimation of geometrical theory of diffraction model," *IET Radar, Sonar Navigat.*, vol. 8, no. 4, pp. 318–326, 2013.

[4] Y. Q. Zou, X. Z. Gao, X. Li, and Y. X. Liu, "A matrix pencil algorithm based multiband iterative fusion imaging method," *Sci. Rep.*, vol. 6, Jan. 2016, Art. no. 19440.

[5] H. H. Zhang and R. S. Chen, "Coherent processing and superresolution technique of multi-band radar data based on fast sparse Bayesian learning algorithm," *IEEE Trans. Antennas Propag.*, vol. 62, no. 12, pp. 6217–6227, Dec. 2014.

[6] Y. Zhang, T. Wang, H. Zhao, Y. Zhang, and H. Zhao, "Multiple radar subbands fusion algorithm based on support vector regression in complex noise environment," *IEEE Trans. Antennas Propag.*, vol. 66, no. 1, pp. 381–392, Jan. 2018.

[7] L. D. Vann, K. M. Cuomo, J. E. Piou, and J. T. Mayhan, "Multisensor fusion processing for enhanced radar imaging," DTIC, Fort Belvoir, VA, USA, Tech. Rep. 1056, 2000.

[8] J. Tian, J. Sun, G. Wang, Y. Wang, and W. Tan, "Multiband radar signal coherent fusion processing with IAA and apFFT," *IEEE Signal Process. Lett.*, vol. 20, no. 5, pp. 463–466, May 2013.

[9] P. V. Dorp, R. Ebeling, and A. G. Huizing, "High resolution radar imaging using coherent multiband processing techniques," in *Proc. IEEE Radar Conf.*, May 2010, pp. 981–986.

[10] F. Ye, F. He, and Z. Sun, "Radar signal level fusion imaging," in *Proc. IEEE Int. Geosci. Remote Sens. Symp. (IGARSS)*, vol. 4. Jul. 2008, pp. IV-1288–IV-1291.

[11] Z. Li, S. Papson, and R. M. Narayanan, "Data-level fusion of multilook inverse synthetic aperture radar images," *IEEE Trans. Geosci. Remote Sens.*, vol. 46, no. 5, pp. 1394–1406, May 2008.

[12] J. H. G. Ender, "The meaning of k-space for classical and advanced SAR techniques," in *Proc. Int. Symp. Phys. Signal Image Process. (PSIP)*, Marseille, France, Jan. 2001, pp. 23–38.

[13] K. Langenberg *et al.*, "Principles of microwave imaging and inverse scattering," *EARSeL Adv. Remote Sens.*, vol. 2, no. 1, pp. 163–186, 1993.

[14] G. Gennarelli, I. Catapano, F. Soldovieri, and R. Persico, "On the achievable imaging performance in full 3-D linear inverse scattering," *IEEE Trans. Antennas Propag.*, vol. 63, no. 3, pp. 1150–1155, Mar. 2015.

[15] J. Wang, H. Cetinkaya, and A. G. Yarovoy, "Comparison of CSAR, E-CSAR and planar circular array for 3-D imaging," in *Proc. IET Int. Radar Conf.*, 2015, pp. 1–5.

[16] A. Papoulis, *Systems and Transforms With Applications in Optics*. Malabar, FL, USA: Robert Krieger, 1968.

[17] J. M. Lopez-Sanchez and J. Fortuny-Guasch, "3-D radar imaging using range migration techniques," *IEEE Trans. Antennas Propag.*, vol. 48, no. 5, pp. 728–737, May 2000.

[18] A. C. Kak and M. Slaney, *Principles of Computerized Tomographic Imaging*. Piscataway, NJ, USA: IEEE Press, 1988.

[19] P. Stoica and Y. Selen, "Model-order selection: A review of information criterion rules," *IEEE Signal Process. Mag.*, vol. 21, no. 4, pp. 36–47, Jul. 2004.

[20] R. Roy and T. Kailath, "Esprit-estimation of signal parameters via rotational invariance techniques," *IEEE Trans. Acoust., Speech, Signal Process.*, vol. 37, no. 7, pp. 984–995, Jul. 1989.

[21] T. K. Sarkar and O. Pereira, "Using the matrix pencil method to estimate the parameters of a sum of complex exponentials," *IEEE Antennas Propag. Mag.*, vol. 37, no. 1, pp. 48–55, Feb. 1995.

[22] H. Liu and M. Sato, "Determination of the phase center position and delay of a Vivaldi antenna," *IEICE Electron. Exp.*, vol. 10, no. 21, p. 20130573, 2013.

[23] E. G. Plaza, G. Leon, S. Loredo, and L. F. Herran, "Calculating the phase center of an antenna: A simple experimental method based on linear near-field measurements," *IEEE Antennas Propag. Mag.*, vol. 59, no. 5, pp. 130–175, Oct. 2017.

[24] J. W. Wiggins, "Kirchhoff integral extrapolation and migration of nonplanar data," *Geophysics*, vol. 49, no. 8, pp. 1239–1248, 1984.

[25] L. Greengard and J.-Y. Lee, "Accelerating the nonuniform fast Fourier transform," *SIAM Rev.*, vol. 46, no. 3, pp. 443–454, 2004.

[26] A. Dutt and V. Rokhlin, "Fast Fourier transforms for nonequispaced data," *SIAM J. Sci. Comput.*, vol. 14, no. 6, pp. 1368–1393, 1993.

[27] R. Solimene, A. Buonanno, F. Soldovieri, and R. Pierri, "Physical optics imaging of 3-D PEC objects: Vector and multipolarized approaches," *IEEE Trans. Geosci. Remote Sens.*, vol. 48, no. 4, pp. 1799–1808, Apr. 2010.

[28] X. Zhuge and A. Yarovoy, "Design of low profile antipodal Vivaldi antenna for ultra-wideband near-field imaging," in *Proc. 4th Eur. Conf. Antennas Propag. (EuCAP)*, Apr. 2012, pp. 1–5.

[29] K. Naishadham and J. E. Piou, "A robust state space model for the characterization of extended returns in radar target signatures," *IEEE Trans. Antennas Propag.*, vol. 56, no. 6, pp. 1742–1751, Jun. 2008.

[30] W. Zhang and A. Hoorfar, "Three-dimensional real-time through-the-wall radar imaging with diffraction tomographic algorithm," *IEEE Trans. Geosci. Remote Sens.*, vol. 51, no. 7, pp. 4155–4163, Jul. 2013.
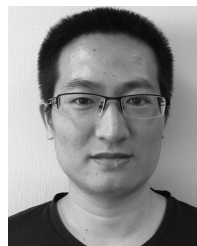
Jianping Wang received the B.Sc. degree in electrical engineering from the North China University of Technology, Beijing, China, in 2009, and the M.Sc. degree in electrical engineering from the Beijing Institute of Technology, Beijing, in 2012. He is currently pursuing the Ph.D. degree with the Delft University of Technology, Delft, The Netherlands.

From 2012 to 2013, he was a Research Associate with the University of New South Wales, Sydney, NSW, Australia, where he was involved in frequency-modulated continuous wave synthetic aperture radar signal processing for formation flying satellites. In 2013, he joined the Group of Microwave Sensing, Signals and Systems, Delft University of Technology. His research interests include radar imaging, signal processing, and antenna array design.

Pascal Aubry received the D.E.S.S. degree in electronics and automatics from Pierre-and-Marie-Curie University, Paris, France, in 1993.

He was a Young Graduate Trainee with the European Space Research and Technology Centre, Noordwijk, The Netherlands, in 1996, where he was involved in antenna measurements. Since 1997, he has been with the International Research Centre for Telecommunications and Radar, Delft University of Technology, Delft, The Netherlands. His research interests include antenna measurement techniques, radar system testing, and signal processing and analysis.
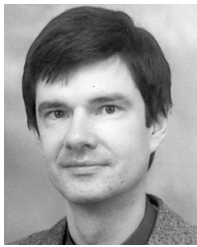
Alexander Yarovoy (F'15) received the Diploma degree (Hons.) in radiophysics and electronics, and the Candidate of Physics and Mathematical Science and Doctor of Physics and Mathematical Science degrees in radiophysics from Kharkov State University, Kharkov, Ukraine, in 1984, 1987, and 1994, respectively.

In 1987, he joined the Department of Radiophysics, Kharkov State University, as a Researcher, and then became a Professor in 1997. From 1994 to 1996, he was with the Technical University of Ilmenau, Ilmenau, Germany, as a Visiting Researcher. Since 1999, he has been with the Delft University of Technology, Delft, The Netherlands, where he has been the Chair of the Group of Microwave Sensing, Signals and Systems since 2009. He has authored or co-authored over 250 scientific or technical papers and 14 book chapters. He holds four patents. His research interests include ultrawideband microwave technology and its applications (particularly radars) and applied electromagnetics (particularly an ultrawideband antennas).

Dr. Yarovoy was a recipient of the European Microwave Week Radar Award for the paper that best advances the state of the art in radar technology in 2001 (together with L. P. Ligthart and P. van Genderen) and in 2012 (together with T. Savelyev). In 2010, together with D. Caratelli, he received the best paper award of the Applied Computational Electromagnetic Society. He served as the Chair and TPC Chair of the 5th European Radar Conference (EuRAD 08), Amsterdam, The Netherlands, as well as the Secretary of the 1st European Radar Conference (EuRAD 04), Amsterdam. He also served as the Co-Chair and TPC Chair of the 10th International Conference on Ground Penetrating Radar (GPR 2004), Delft. Since 2008, he has been serving as the Director of the European Microwave Association. He served as the guest editor of five special issues of the IEEE TRANSACTIONS and other journals. Since 2011, he has been an Associate Editor of the *International Journal of Microwave and Wireless Technologies*.